Electromagnetic Modeling for Microwave Imaging of Cylindrical Buried Inhomogeneities

LUC CHOMMELOUX, CHRISTIAN PICHOT, AND JEAN-CHARLES BOLOMEY

Abstract — **Many diagnostic techniques in geophysics and civil engineering are based on the interaction of electromagnetic waves with objects buried in homogeneous or stratified media. Most of the investigations are concerned with the detection of buried objects, but a few papers have dealt with the problem of identifying the objects.**

The proposed method is based on the integral representation for a plane wave incident on a lossy half-space containing a cylindrical object of arbitrary cross section and electrical properties. The induced current distribution in the object is obtained from the backscattered field measurement in amplitude and phase. In order to improve the spatial resolution of the image, the scattered field is measured for different plane wave incidences and frequencies. Results of numerical simulations concerning the shape and size of the object for different values of soil electromagnetic parameters are presented in this paper.

I. Introduction

THE DETECTION and identification of buried inhomogeneities using electromagnetic waves are areas of current importance for geophysical or civil engineering purposes. An example is the detection of pipes and cables, some of which may consist entirely of plastic materials. For such cases, conventional metal detectors fail and one must employ alternative means of investigation. During the past few years, some papers have been concerned with this problem. The possibility of identifying nonmetallic objects buried at shallow depths below the ground has been demonstrated using an FM radar in the 2–4-GHz range [1], a step frequency radar in the 300–700-MHz range [2], and impulse radars [3]–[5]. The principle of identifying buried objects by the microwave holographic imaging method has been established in recent years. Richards *et al.* [6] proposed a technique able to produce images of gas pipes at depths up to 0.25 m below the ground with a 0.95-GHz radiation, but since the method employs only a single frequency, it does not provide a high vertical resolution.

Osumi and Ueno recently developed a microwave imaging method [7] which they applied to underground imaging [8]. The reflectance of the buried object is reconstructed from the knowledge of the scattered pulses measured at a collection of points in the air, so that both vertical and horizontal resolutions are improved.

Our approach is based on recent work in medical applications concerning active microwave and acoustic imaging [9]–[12], [31]. Reconstruction algorithms have been extended to the case of inhomogeneities embedded in the soil by taking into account the presence of the air–soil interface and by measuring the backscattered field in air. The simulation algorithm can be divided into two parts: *the direct problem* — simulation of experimental measurement of the diffracted field, and *the inverse problem* — reconstruction of a function characteristic of the inhomogeneity from knowledge of the diffracted field for different incidences and frequencies.

In this paper, we first present the theoretical formulation upon which the imaging method is based. We then describe the main steps of the algorithm (direct and inverse problem). Finally, numerical results concerning the size and the shape of the object for different soils are presented.

II. Theoretical Formulation

We consider a cylindrical inhomogeneity embedded in a lossy homogeneous half-space (Fig. 1). Media 1 and 3 are air and soil, respectively, and are characterized by dielectric permittivity, and conductivity ϵ_1, σ_1 and ϵ_3, σ_3, respectively. The object is characterized by $\epsilon_s(x, y)$, $\sigma_s(x, y)$. The object of arbitrary cross section $S(x, y)$ is illuminated by an incident plane wave whose electric field vector is perpendicular to the incidence plane (TM case). For any point (x, y) inside or outside the object, the total electric field can be expressed as the sum of the incident field E_z^I (defined as the field when the object is removed) and diffracted field ψ

$$E_z(x, y) = E_z^I(x, y) + \psi(x, y). \tag{1}$$

Because of the size of the object, whose dimensions are about one wavelength (resonance domain), an exact formulation of the diffracted field must be employed. Analytical formulations which are available only in particular cases (buried circular cylinder [13], for example) have been rejected.

An exact representation for the z component of the diffracted field at a point (x, y) (for a time factor $e^{-i\omega t}$) is

Manuscript received October 29, 1985; revised May 1, 1986.

The authors are with Groupe d'Electromagnétisme, Laboratoire des Signaux et Systèmes, C.N.R.S-E.S.E., Plateau du Moulon, 91190 Gif-sur-Yvette, France.

IEEE Log Number 8609848.

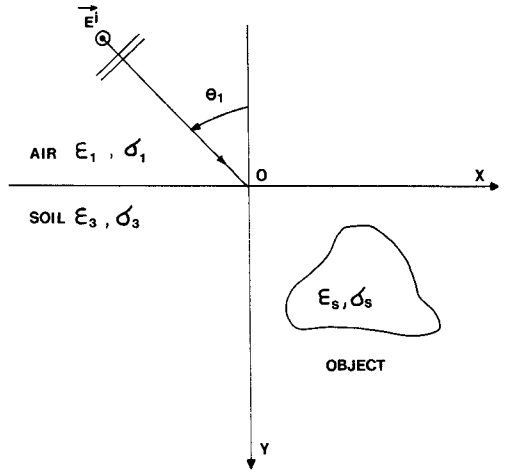

Fig. 1. Geometry of the problem in the (x, y) plane.

given by [14]

$$\psi(x, y) = \int\int_S \left[k_S^2(x', y') - k_3^2\right] E_z(x', y') \cdot G(x, y; x', y')\, dx'\, dy' \quad (2)$$

where

$$k_j^2(x, y) = \omega^2 \varepsilon_j(x, y)\mu_0 + i\omega\mu_0\sigma_j(x, y), \qquad j = 1, 3, S \quad (3)$$

and S is the region $y > 0$ for which the medium parameters differ from those of the background medium.

$G(x, y; x', y')$ is the Green's function, which can be interpreted as the electric field created at a point (x, y) by a line source of current situated at a point (x', y'). $G(x, y; x', y')$ is given by its integral expression (see Appendix)

$$G(x, y; x', y') \quad (\text{for } y' > 0) = \begin{cases} \displaystyle\int_{-\infty}^{+\infty} \frac{i}{\tilde{\gamma}_1 + \tilde{\gamma}_3} e^{-i\tilde{\gamma}_1 y} e^{i\tilde{\gamma}_3 y'} e^{2i\pi\nu(x-x')}\, d\nu \\ \qquad (\text{for } y < 0) \\ \displaystyle\int_{-\infty}^{+\infty} \frac{i}{2\tilde{\gamma}_3} \left[e^{i\tilde{\gamma}_3 |y-y'|} + \frac{\tilde{\gamma}_3 - \tilde{\gamma}_1}{\tilde{\gamma}_3 + \tilde{\gamma}_1} e^{i\tilde{\gamma}_3 (y+y')} \right] e^{2i\pi\nu(x-x')}\, d\nu \\ \qquad (\text{for } y > 0). \end{cases} \quad (4)$$

We shall note

$$G(x, y; x', y') = \begin{cases} G_1(x, y; x', y') & (\text{for } y < 0) \\ G_3(x, y; x', y') & (\text{for } y > 0) \end{cases} \quad (5)$$

with

$$\tilde{\gamma}_j^2 = k_j^2 - 4\pi^2\nu^2, \qquad j = 1, 3 \text{ and } \operatorname{Im}(\tilde{\gamma}_j) \le 0. \quad (6)$$

Because of the air–soil interface, the incident plane wave generates two waves: a reflected one (for $y < 0$) and a transmitted one (for $y > 0$), in the absence of inhomogeneity:

$$E_z^{\mathrm{I}}(x, y) = \begin{cases} e^{ik_1(x\sin\theta_1 + y\cos\theta_1)} + Re^{ik_1(x\sin\theta_1 - y\cos\theta_1)} \\ \qquad (\text{for } y < 0) \\ Te^{ik_3(x\sin\theta_3 + y\cos\theta_3)} \\ \qquad (\text{for } y > 0). \end{cases} \quad (7)$$

We shall note

$$E_z^{\mathrm{I}}(x, y) = \begin{cases} E_z^i(x, y) + E_z^r(x, y) & (\text{for } y < 0) \\ E_z^t(x, y) & (\text{for } y > 0) \end{cases} \quad (8)$$

with

$$\left.\begin{aligned} R &= \frac{1-n}{1+n} \qquad T = \frac{2}{1+n} \\ n &= \frac{\cos\theta_3}{\cos\theta_1} \qquad \sqrt{\frac{\epsilon_3 + i\sigma_3/\omega}{\epsilon_1 + i\sigma_1/\omega}} \end{aligned}\right\} \quad (\text{Fresnel's relations}) \quad (9)$$

and

$$k_1 \sin\theta_1 = k_3 \cos\theta_3 \qquad (\text{Snell's law}).$$

The reconstruction method is based on the measure of the diffracted field in the air on a probing line of finite length, parallel to the air–soil interface. Let us consider the expression of the diffracted field for $y = y_1$ $(y_1 < 0)$ when the object is illuminated by a plane wave with an electric field amplitude of 1V/m and an incidence θ_1 (Fig. 1)

$$\psi(x, y_1) = \int\int_S k_3^2 E_z^t(x', y') K(x', y') \cdot G_1(x, y_1; x', y')\, dx'\, dy' \quad (10)$$

where

$$K(x', y') = \left[\frac{k_S^2(x', y')}{k_3^2} - 1\right]\left[1 + \frac{\psi(x', y')}{E_z^t(x', y')}\right] \quad (11)$$

represents the normalized polarization currents. By substituting (4) and (7) into (10) and defining the Fourier transform of (x, y_1) with respect to x as follows:

$$\hat{\psi}(\nu, y_1) = \int_{-\infty}^{+\infty} \psi(x, y_1) e^{-2i\pi\nu x}\, dx \quad (12)$$

we obtain

$$\hat{\psi}(\nu, y_1) = \frac{ik_3^2 T e^{-i\tilde{\gamma}_1 y_1}}{(\tilde{\gamma}_1 + \tilde{\gamma}_3)} \int\int_S K(x', y') \cdot e^{-2i\pi\left[\left(\nu - \frac{k_3}{2\pi}\sin\theta_3\right)x' - \frac{1}{2\pi}(\tilde{\gamma}_3 + k_3\cos\theta_3)y'\right]} dx'\, dy'. \quad (13)$$

Since $K(x', y')$ is zero outside the object, we can extend the integral to infinity. In order to define the usual 2-D Fourier transform, we must consider a real coordinate system in the Fourier plane; this is realized by the assump-

tion $\sigma_3 = 0$ in the inverse problem. Thus, we can define

$$\begin{cases} \alpha(\nu,\theta_3) = \nu - \dfrac{k_3}{2\pi}\sin\theta_3 & \in \mathbb{R} \\ \beta(\nu,\theta_3) = -\dfrac{1}{2\pi}(\tilde{\gamma}_3 + k_3\cos\theta_3) & \in \mathbb{R}\left(|\nu| \geq \dfrac{k_1}{2\pi}\right) \\ & \text{(visible spectrum)} \\ k_3^2 = \omega^2\mu_0\epsilon_3 & \in \mathbb{R} \end{cases} \tag{14}$$

and (13) becomes

$$\hat{K}(\alpha(\nu,\theta_3),\beta(\nu,\theta_3)) = -i\frac{(\tilde{\gamma}_1+\tilde{\gamma}_3)}{k_3^2 T}e^{i\tilde{\gamma}_1 y_1}\hat{\psi}(\nu, y_1) \tag{15}$$

where

$$\hat{K}(\alpha,\beta) = \int_{-\infty}^{+\infty}\int_{-\infty}^{+\infty} K(x,y)e^{-2i\pi(\alpha x+\beta y)}\,dx\,dy \tag{16}$$

denotes the 2-D Fourier transform of $K(x, y)$.

So medium 3 is assumed to be lossless for the object reconstruction, but losses are taken into account in the simulation of the direct problem. This assumption simplifies the Fourier relation between the diffracted field and the normalized polarization current. The extension to lossy media could be carried out using Laplace or Fourier transforms in the complex plane. The relation (15) states that, for $|\nu| \leq k_1/2\pi$, the Fourier transform of the diffracted field for an incidence θ_1 provides information on the 2-D Fourier transform of the polarization current distribution on a circular arc $S(\theta_3)$ defined by (14). Fig. 2 shows the circular arc $S(\theta_3)$ in the Fourier plane corresponding to the normal incidence ($\theta_1 = \theta_3 = 0$). This result is very close to the generalized Radon theorem, which has been formulated in recent papers [15], [16].

The quality of object reconstruction will be determined by the impulse $h(x, y)$ of the system. The reconstructed spatial distribution is given by the following convolution product:

$$\tilde{K}(x,y) = K(x,y) * h(x,y). \tag{17}$$

We examine the case where the incident plane is normally incident ($\theta_1 = \theta_3 = 0$).

In order to determine the impulse response of the system, we consider that $K(x, y)$ is a Dirac distribution. Therefore

$$K(x,y) = \delta(x,y) \tag{18}$$

and

$$\hat{K}(\alpha,\beta) = 1. \tag{19}$$

In the case of normal incidence, the circular arc in the Fourier plane is defined by

$$\begin{cases} \alpha(\nu,0) = \nu \\ \beta(\nu,0) = -\dfrac{1}{2\pi}(\tilde{\gamma}_3 + k_3) \\ |\nu| \leq \dfrac{k_1}{2\pi}. \end{cases} \tag{20}$$

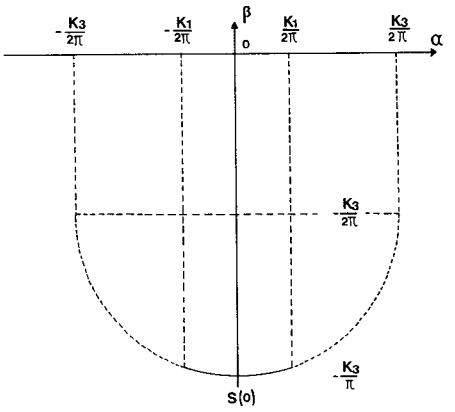

Fig. 2. Circular arc $S(0)$ in the Fourier plane over which $\hat{K}(\alpha,\beta)$ is determined for the normal incidence case, i.e., $\theta_1 = 0$, and $\epsilon_3 > \epsilon_1$. —— Nonevanescent spectrum. ----- Evanescent spectrum.

Thus, $\tilde{K}(x, y)$ is obtained by taking the inverse 2-D Fourier transform of $\hat{\tilde{K}}(\alpha,\beta)$, defined by

$$\hat{\tilde{K}}(\alpha,\beta) = \begin{cases} 1, & \text{for } \begin{cases} \alpha = \alpha(\nu,0) \\ \beta = \beta(\nu,0) \end{cases} |\nu| \leq \dfrac{k_1}{2\pi} \\ 0, & \text{elsewhere} \end{cases} \tag{21}$$

and

$$\tilde{K}(x,y) = \int_{-\infty}^{+\infty}\int_{-\infty}^{+\infty}\hat{\tilde{K}}(\alpha,\beta)e^{2i\pi(\alpha x+\beta y)}d\alpha\,d\beta. \tag{22}$$

By performing a simple change of variable, we obtain

$$h(x,y) = k_3\int_{-k_1/2\pi}^{k_1/2\pi}\frac{1}{\tilde{\gamma}_3}e^{-i(\tilde{\gamma}_3+k_3)y}e^{2i\pi\nu x}\,d\nu. \tag{23}$$

The amplitude of this integral is shown in Fig. 3, and the resolution (width at half height of the central lobe) is seen to be better along the x direction than along y; we can estimate them to be $\delta_x = 0.6\lambda_1$ and $\delta_y = 8\lambda_1$ (λ_1 denoting the wavelength in vacuum; at 3 GHz, $\delta_x = 6$ cm and $\delta_y = 80$ cm). One notes that the air–soil interface is not discerned in the reconstructed image. Indeed, the interface is not discerned in the reconstruction algorithm with formula (15). That could be rigorously demonstrated using a point source located in the soil at point (x_s, y_s). After some calculations, one obtains for the reconstructed image

$$\tilde{K}(x,y) = \frac{e^{-ik_3 y_s}}{k_3 T}h(x-x_s, y-y_s)$$

where $h(x, y)$ is the impulse response in the unbounded soil (eq. (23)) and T is the transmission coefficient of the air–soil interface (eq. (9)).

While the transversal resolution δ_x is quite satisfactory, the longitudinal one, δ_y, needs to be improved. Thus, the main problem is now the improvement of the knowledge of $\hat{K}(\alpha,\beta)$. To obtain more information in the Fourier domain, we consider the incidence and frequency variation of the incident plane wave.

In medical applications, sources and receivers are free to rotate around the object, and a good symmetric impulse response can therefore be obtained. In our case, we cannot

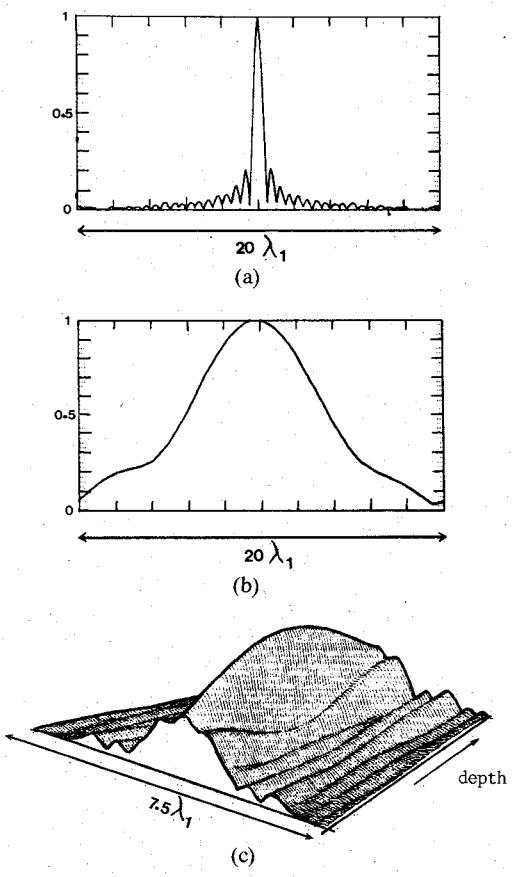

Fig. 3. Example of reconstuction at 3 GHz of $|h(x,y)|$ for $\epsilon_{r_3}=15$ and $\sigma_3=5\times10^{-2}$ S/m. (a) Normalized transversal section. (b) Normalized longitudinal section. (c) 3-D representation ($\delta_x\simeq 6$ cm and $\delta_y\simeq 80$ cm).

adopt the same procedure. One method consists in measuring the diffracted field on a fixed probing line for plane waves with the angle of incidence varying from $-\pi/2$ to $+\pi/2$. Fig. 4 shows three circular arcs $S(\theta_1)$ corresponding to incidence angles of $-\pi/2, 0, +\pi/2$.

By combining all the incidence information in the Fourier domain, we obtain

$$\hat{\hat{K}}(\alpha,\beta)=\sum_{j=1}^{N_I}\hat{K}\big(\theta_j;\alpha(\nu,\theta_j),\beta(\nu,\theta_j)\big) \tag{24}$$

where N_I denotes the number of incidence angles. By performing the inverse 2-D Fourier transform of the resulting information, the reconstruction is given by

$$\tilde{K}(x,y)=\sum_{j=1}^{N_I}K(\theta_j;x,y)*h(\theta_j;x,y) \tag{25}$$

where

$$K(\theta_j;x,y)=\left[\frac{k_S^2(x,y)}{k_3^2-1}\right]\left[1+\frac{\psi(\theta_j;x,y)}{E_z^t(\theta_j;x,y)}\right] \tag{26}$$

and

$$h(\theta_j;x,y)=k_3\int_{-k_1/2\pi}^{k_1/2\pi}\frac{1}{\tilde{\gamma}_3}e^{-i(\tilde{\gamma}_3+k_3\cos\theta_{3j})}e^{2i\pi(\nu-k_3/2\pi\sin\theta_{3j})}\,d\nu. \tag{27}$$

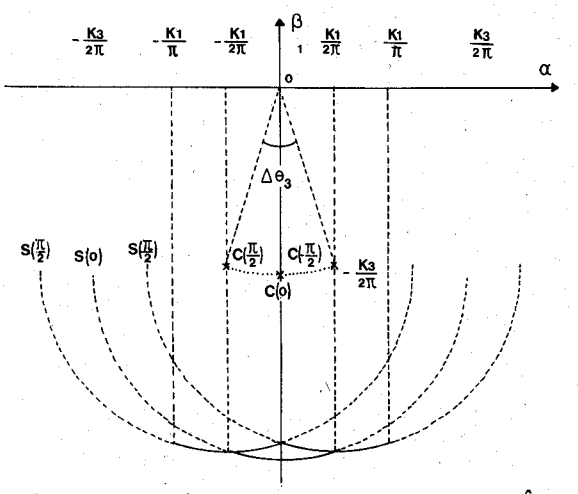

Fig. 4. Circular arcs $S(\theta_1)$ in the Fourier plane over which $\hat{K}(\alpha,\beta)$ is determined when θ_1 takes the values $-\pi/2$, 0, $+\pi/2$; the centers $C(\theta_1)$ of the circle arcs lie on a circle arc of radius $k_3/2\pi$ centered at (0,0). —— Nonevanescent spectrum. ----- Evanescent spectrum. ····· Variation domain of $C(\theta_1)$.

Angles θ_1 and θ_3 are related by Snell's law (9), so that values of θ_3, when θ_1 varies from $-\pi/2$ to $+\pi/2$, belong to the interval

$$\Delta\theta_3=\left[-\arcsin\left(\frac{k_1}{k_3}\right),\arcsin\left(\frac{k_1}{k_3}\right)\right].$$

Centers of the supports $C(\theta_1)$ (see Fig. 4) move on a circular arc of radius $k_3/2\pi$ defined by an angle of 2 $\arcsin(k_1/k_3)$. The spatial frequencies belong to the following intervals:

$$\begin{cases}\Delta\alpha=\left[-\dfrac{k_1}{\pi},\dfrac{k_1}{\pi}\right]\\ \Delta\beta=\left]-\dfrac{k_3}{\pi},-\dfrac{\sqrt{k_3^2-k_1^2}}{\pi}\right[\end{cases}\quad\text{for}\quad\begin{cases}|\theta_3|<\arcsin\left(\dfrac{k_1}{k_3}\right)\\ |\nu|\le\dfrac{k_1}{2\pi}.\end{cases} \tag{28}$$

The more (ϵ_1,σ_1) and (ϵ_3,σ_3) differ, the more the information in the Fourier domain is reduced. The Fourier domain we fill up is in fact limited to such a small area that it is necessary to use some other technique to extend the knowledge of $\hat{K}(\alpha,\beta)$. The quality of the spatial impulse response can be improved by processing data obtained from measurements performed at different frequencies [17].

Fig. 5 shows two circular arcs $S(\omega)$ corresponding to frequencies ω_1,ω_2, with $\omega_1>\omega_2$ for normal incidence. By combining information in the Fourier domain, a similar relation is obtained:

$$\hat{\hat{K}}(\alpha,\beta)=\sum_{i=1}^{N_F}K\big(\omega_i;\alpha(\nu,\omega_i),\beta(\nu,\omega_i)\big). \tag{29}$$

Thus, taking the inverse 2-D Fourier transform of $\hat{\hat{K}}(\alpha,\beta)$

$$\tilde{K}(x,y)=\sum_{i=1}^{N_F}K(\omega_i;x,y)*h(w_i;x,y) \tag{30}$$

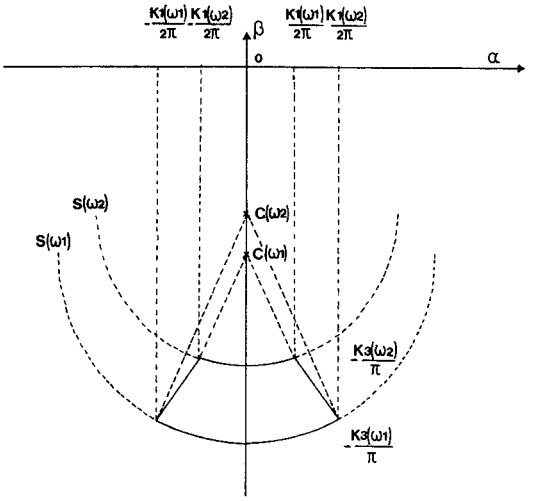

Fig. 5. Circular arcs $S(\omega)$ in the Fourier plane over which $\hat{K}(\alpha,\beta)$ is determined when the frequency varies from ω_1 to ω_2. ($\omega_2 < \omega_1$) in the case of the normal incidence ($\theta_1 = 0$). —— Nonevanescent spectrum. ----- Evanescent spectrum.

with

$$K(\omega_i;x,y)=\left[\frac{k_S^2(\omega_i;x,y)}{k_3^2(\omega_i)}-1\right]\left[1+\frac{\psi(\omega_i;x,y)}{E_z^t(\omega_i;x,y)}\right] \quad (31)$$

and

$$h(\omega_i;x,y)=k_3(\omega_i)\cdot\int_{-k_1(\omega_i)/2\pi}^{+k_1(\omega_i)/2\pi}e^{-\imath(\tilde{\gamma}_3(\omega_i)+k_3(\omega_i))y}\frac{e^{2\imath\pi\nu x}}{\tilde{\gamma}_3(\omega_i)}d\nu. \quad (32)$$

By combining in the Fourier plane information obtained from measurements performed at N_I incidences and N_F frequencies, we obtain a reconstructed $\tilde{K}(x,y)$, given by

$$\tilde{K}(x,y)=\sum_{i=1}^{N_F}\sum_{j=1}^{N_I}K(\omega_i;\theta_j;x,y)*h(\omega_i;\theta_j;x,y). \quad (33)$$

III. Numerical Aspects

A. Description of the Algorithm

In this section, we test the algorithm as it is indicated in Fig. 6. Using the integral formulation (2), the evaluation of the diffracted field on a probing line requires first a knowledge of the total electric field inside the inhomogeneity. In order to calculate this field, we have to solve a Fredholm's integral equation of the second kind by means of the method of moments [14], [18]–[22]. This leads us to the solution of a system of linear equations with rank N (N representing the total number of elementary cells constituting the object). Cells have to be taken sufficiently small so that the dielectric constant and the electric field can be considered constant over each cell. The total field in the object is obtained after inversion of this system by a Gauss–Jordan algorithm. The diffracted field can then be computed for any point in the space by using the appropriate Green's function. The accuracy of the numerical

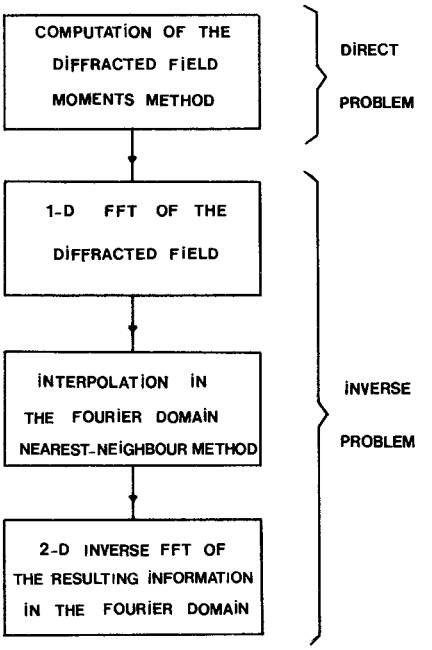

Fig. 6. Main steps of the algorithm used for buried object imaging (direct and inverse problem).

approximations has been checked by making computations for the same object with different values of Δx (Δx denoting the size of an elementary square cell). Results with an accuracy of about 5 percent are obtained for a sampling interval Δ_x of $\lambda_3/5$, where

$$\lambda_3=\frac{\lambda_1}{\sqrt{\epsilon_{r_3}}} \quad \text{and} \quad \epsilon_{r_3}=\frac{\epsilon_3}{\epsilon_1}.$$

Briefly, the reconstruction algorithm based on Fourier inversion formulas consists of three major steps.

1) 1-D Fourier Transforms: The first step of the algorithm is to compute the 1-D Fourier transform of the diffracted field measured in the air at angles θ_{1_j}, $j=1, N_I$ and frequencies ω_i, $i=1, N_F$. The sampled diffracted field $\psi_N(x)$, measured at $2N+1$ points with a sampling interval Δx, can be written as

$$\psi_N(x)=S_N(x)\psi(x). \quad (34)$$

Here, $\psi(x)$ denotes the diffracted field for an incidence θ_1 at a frequency ω measured on a probing line of infinite length situated at y_1 above the air–soil interface, and $S_N(x)$ is a distribution defined by

$$S_N(x)=\sum_{m=-N}^{m=N}\delta\left(\frac{x}{\Delta x}-m\right)=\sum_{m=-N}^{m=N}\Delta x\delta(x-m\Delta x) \quad (35)$$

where $\delta(x)$ denotes the Dirac distribution.

The next step is to take the Fourier transform of $\psi_N(x)$ so that

$$\hat{\psi}_N(\nu)=\sum_{m=-N}^{m=N}\Delta x\psi(m\Delta x)e^{-2\imath\pi\nu m\Delta x} \quad (36)$$

or

$$\hat{\psi}_N(\nu) = \Delta x \hat{\psi}(\nu) * \frac{\sin[\pi\nu(2N+1)\Delta x]}{\sin[\pi\nu\Delta x]}. \quad (37)$$

Thus, $\hat{\psi}_N(\nu)$ is a periodic function of period $1/\Delta x$. In order to avoid problems of aliasing in the computation of $\hat{\psi}_N(\nu)$, we have to sample with

$$\Delta x \leq \frac{\lambda_1}{2}. \quad (38)$$

2) Interpolation in the Fourier Domain: Numerically, $\hat{\psi}_N(\nu)$ is computed by a fast Fourier transform algorithm. The Fourier plane is filled by methods previously described, and the interpolation from the given circular arcs to the Cartesian grid is realized by the nearest neighbor's method. Other methods of interpolation which have been successfully employed in object reconstruction [15], [23]–[25] have not yet been used.

3) Inverse 2-D Fourier Transform of $\hat{\tilde{K}}(\alpha, \beta)$: If $\hat{\tilde{K}}(\alpha, \beta)$ is sampled with

$$\Delta\alpha = \frac{1}{(2N+1)\Delta x} \quad \text{and} \quad \Delta\beta = \frac{1}{(2M+1)\Delta y}$$

the 2-D inverse fast Fourier transform provides a $(2N+1) \times (2M+1)$ reconstruction given by

$$\tilde{K}_N(x, y) = \frac{\tilde{K}(x, y)}{(2N+1)(2M+1)\Delta x \Delta y} * \left[\frac{\sin(\pi x/\Delta x)\sin(\pi y/\Delta y)}{\pi x/(2N+1)\Delta x \pi y/(2M+1)\Delta y}\right] \quad (39)$$

where $\tilde{K}(x, y)$ is defined by (33). To summarize, the two main sources of error for the inverse problem are the undersampling of the diffracted field and the insufficient length of the probing line.

In these simulations, our primary goal is to evaluate the impulse response of the system, that is, the reconstruction of $K(x, y) = \delta(x - x_s, y - y_s)$ (i.e., a diffracting object located at (x_s, y_s), $y_s > 0$). Then we shall examine the more realistic case of objects embedded in different soils, the size of which is of the order of the wavelength.

Electromagnetic parameters of soil are dependent on soil density, water content, frequency, and temperature. There exist several papers which deal with measurements of conductivity and dielectric constant of different soils at microwave frequencies [26]–[28], and some attempt has been made to model the dielectric behavior of soil–water mixtures in the microwave region [29]. At 3 GHz, the relative permittivity ϵ_{r_3} increases with soil density, and the water content varies from 2.55 (dry sand) to approximately 20 (loamy soil, 13.77 percent moisture) [27]. The conductivity σ_3 is very dependent on water content; for the same soil at 3 GHz, its values are given by $\sigma_3 = 2.6 \times 10^{-3}$ S/m (dry sand) and $\sigma_3 = 4 \times 10^{-1}$ S/m (loamy soil). In order to evaluate signal attenuation in the soil, let us consider the transmitted portion of the incident plane wave

$$E_z^t(x, y) = Te^{ik_3(x\sin\theta_3 + y\cos\theta_3)}. \quad (40)$$

Along the y direction, the attenuation A is given by

$$A = e^{-\mathrm{Im}(k_3\cos\theta_3)y} \quad (41)$$

with $\mathrm{Im}(k_3\cos\theta_3) \geq 0$. The penetration depth δ is therefore defined as

$$\delta = \frac{1}{\mathrm{Im}(k_3\cos\theta_3)} \quad (42)$$

which can be written as

$$\delta = \frac{1}{k_3'' + \dfrac{k_1^2 k_3'' \sin\theta_1}{2(k_3'^2 + k_3''^2)}} \quad (43)$$

with

$$k_3 = k_3' + ik_3'' \quad (44)$$

where

$$k_3' = \frac{1}{\sqrt{2}}\sqrt{\omega^2\mu_0\epsilon_3 + \omega\mu_0(\omega^2\epsilon_3^2 + \sigma_3^2)^{1/2}} \quad (45)$$

and

$$k_3'' = \frac{1}{\sqrt{2}} \frac{\sigma_3\mu_0\omega}{\sqrt{\omega^2\mu_0\epsilon_3 + \omega\mu_0(\omega^2\epsilon_3^2 + \sigma_3^2)^{1/2}}} \quad (46)$$

for a plane wave of incidence θ_1 and circular frequency. For example, in the case of normal incidence, the penetration depth in dry sand and loamy soil are, respectively, $\delta_{(\text{dry sand})} = 3.2$ m; $\delta_{(\text{loamy soil})} = 0.06$ m.

It appears that the two major difficulties with electromagnetic methods are the attenuation in transmission of microwaves in soil and the deterioration of spatial resolution when a lower frequency is used to seek lower attenuation.

B. Numerical Simulations

1) Point Spread Function of the Reconstruction Process: Let us consider a point-diffracting object located at (x_s, y_s) in a soil characterized by $\epsilon_{r_3} = 15$ and $\sigma_3 = 5 \times 10^{-2}$ S/m. Our purpose is to evaluate the improvement in the transverse and longitudinal resolution (δ_x, δ_y) by using measurements performed at different incidences and frequencies. The first simulation is characterized by the following choices: the frequency is fixed at 3 GHz ($\lambda_1 = 10$ cm and the penetration depth for normal incidence is about 40 cm in this case), and the object is characterized by a dielectric permittivity $\epsilon_{r_s} = 2.5$ and conductivity $\sigma_s = 0$ S/m. The diffraction point is buried at a depth $y_s = \lambda_1$ (with $x_s = 0$) and the diffracted field is measured on a probing line of $20\lambda_1$ situated at $y_1 = \lambda_1$ above the air–soil interface. In the case of using an incident field with 25 incidences regularly distributed between the interval $-\pi/2$ and $+\pi/2$ (case 1), the magnitude of the image is shown in Fig. 7. The transversal and longitudinal resolution can be evaluated as $\delta_x = 0.4\lambda_1$ and $\delta_y = 5\lambda_1$.

In order to obtain a quasi-symmetrical resolution along the x and y directions, we make the incidental frequency vary. We consider the following example, where frequency

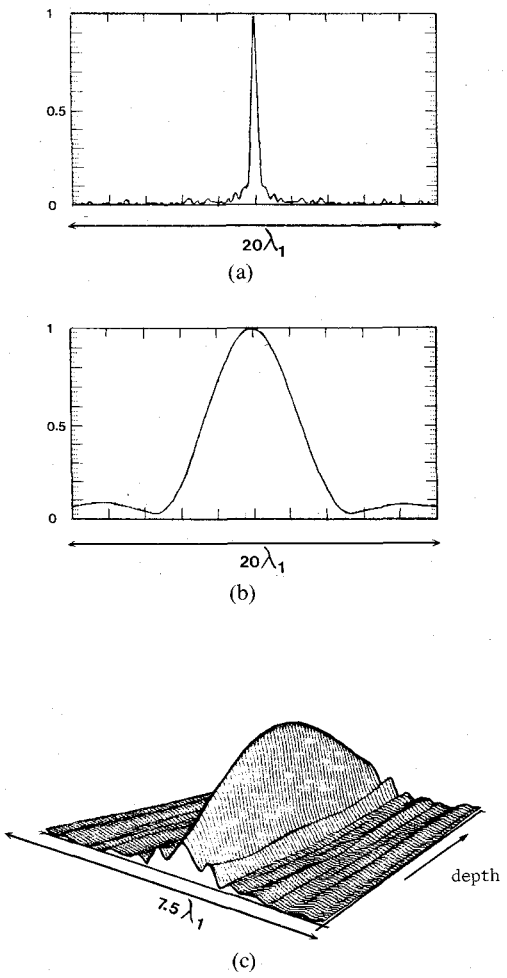

Fig. 7. Impulse response of the reconstruction process obtained at 3 GHz in the case of 25 plane waves with incidences in the interval $]-\pi/2, \pi/2[$. (a) Normalized transversal section. (b) Normalized longitudinal section. (c) 3-D representation ($\delta_x \simeq 4$ cm and $\delta_y \simeq 50$ cm).

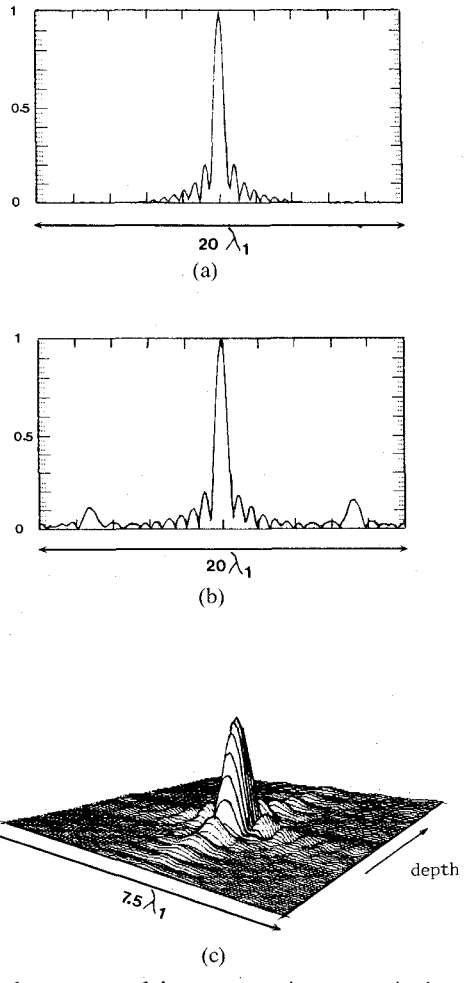

Fig. 8. Impulse response of the reconstruction process in the case of the normal incidence and a frequency variation from 2.43 GHz to 3 GHz. (a) Normalized transversal section. (b) Normalized longitudinal section. (c) 3-D representation ($\delta_x \simeq \delta_y \simeq 6$ cm).

varies in the range 2.43–3 GHz divided in 20 steps of $\Delta f = 0.03$ GHz (incidence is fixed to $\theta_1 = \theta_3 = 0$). The result of such a simulation is shown in Fig. 8. Resolutions along the x and y directions are roughly equal, so that $\delta_x = \delta_y = 0.6\lambda_1$ (λ_1 denoting here the minimal value of the wavelength for the frequency range considered). Fig. 9 permits comparison of the half-height sections of the two images. By combining data obtained from case 1 and case 2 (for every frequency, plane waves with 25 incidences are used to fill up the Fourier plane), we obtain the image which is depicted in Fig. 10, with $\delta_x = 0.4\lambda_1$ and $\delta_y = 0.6\lambda_1$. A filter can be used in the Fourier plane to reduce the sidelobes of the spatial impulse response, but this method generally results in a decrease in resolution [30].

We now evaluate the performance of the algorithm as a function of object electromagnetic parameters $(\epsilon_{r_s}, \sigma_s)$. First, consider the case of two diffracting points buried at the same depth $y_{s1} = y_{s2} = 3\lambda_1$, characterized by the same electromagnetic parameters $\epsilon_{r_{s1}} = \epsilon_{r_{s2}} = 2.5$, $\sigma_{s1} = \sigma_{s2} = 0$ S/m, and separated by a distance of $2\lambda_1$. The reconstruction obtained in magnitude is shown in Fig. 11 (a) and 12 (a). The transversal section of the image provides a

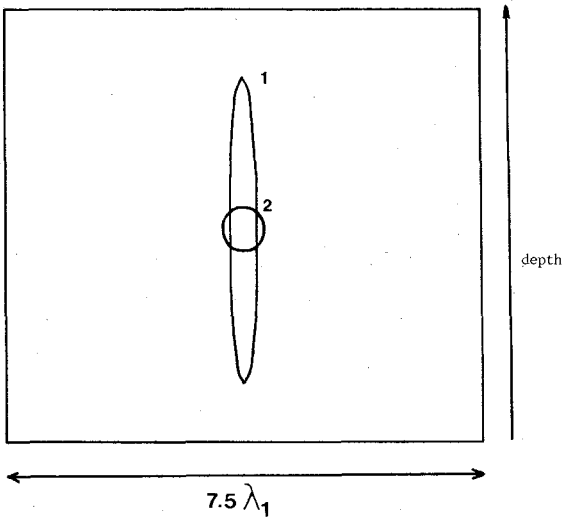

Fig. 9. Comparison of the half-height sections of $|\tilde{K}(x, y)|$ obtained in the two previous cases: 1) incidence varies from $-\pi/2$ to $+\pi/2$, frequency is fixed at 3 GHz; 2) frequency varies from 2.43 GHz to 3 GHz in the case of normal incidence.

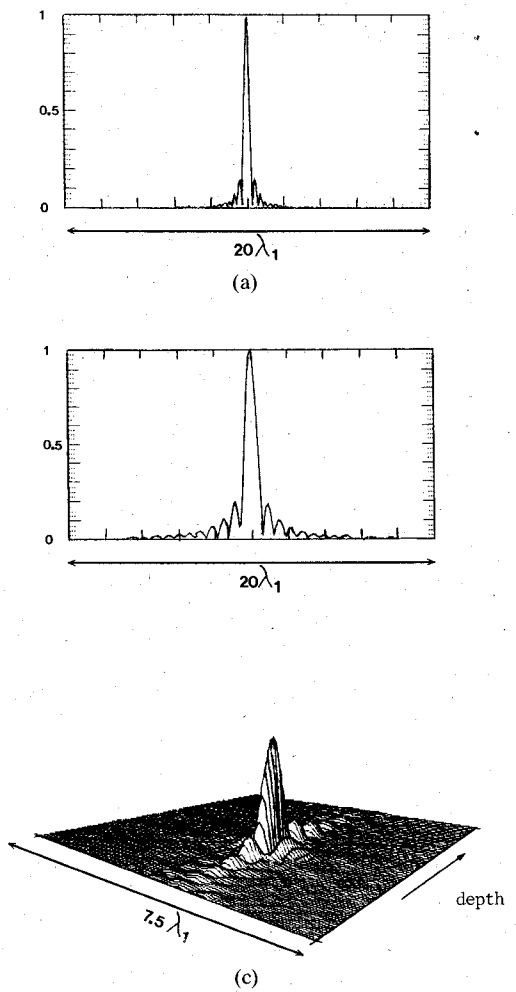

Fig. 10. Impulse response for an incidence variation from $-\pi/2$ to $+\pi/2$ and a frequency variation from 2.43 GHz to 3 GHz ($\delta_x \simeq 4$ cm and $\delta_y \simeq 6$ cm).

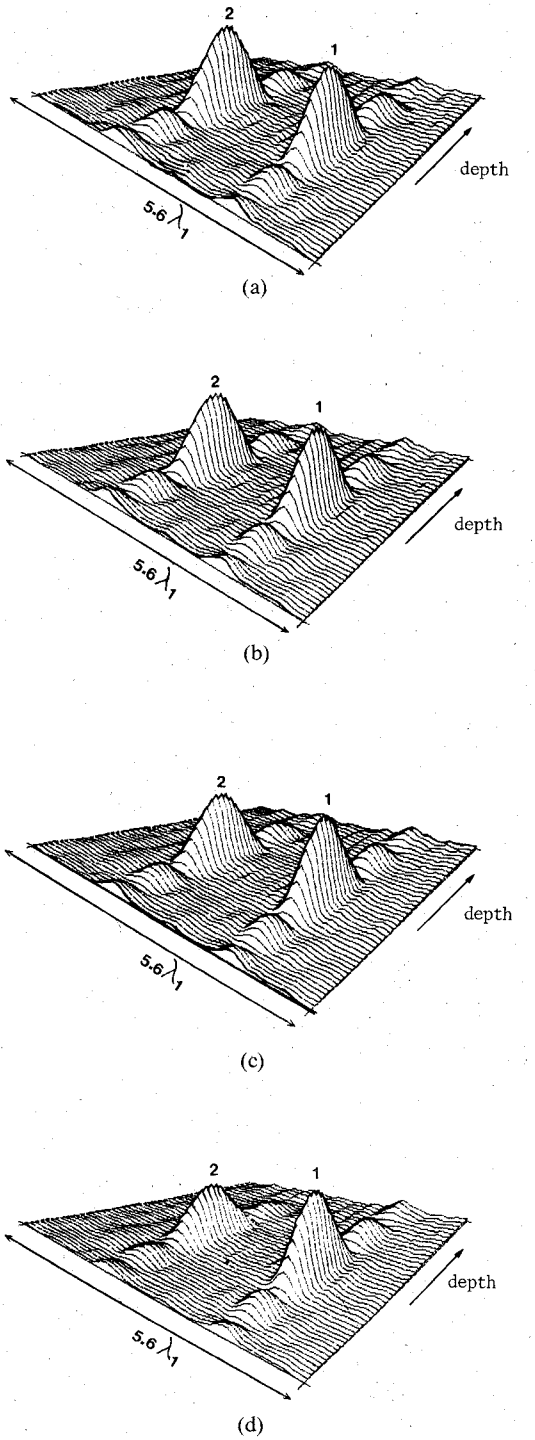

Fig. 11. 3-D representation of $|\tilde{K}(x, y)|$ in the case of two dielectric objects much smaller than the wavelength with different electromagnetic parameters buried at the same depth ($y_{s1} = y_{s2} = 30$ cm). For all cases, $\epsilon_{r_{s1}} = 2.5$, $\sigma_{s1} = \sigma_{s2} = 0$ S/m, and $\epsilon_{r_{s2}} = 2.5$. (a) $\epsilon_{r_{s2}} = 5$. (b) $\epsilon_{sr_2} = 7$. (c) $\epsilon_{r_{s2}} = 9$. (d) Frequency varies from 2.73 GHz to 3 GHz and incidence varies in the range $]-\pi/2, +\pi/2[$.

quantitative evaluation of the reconstructed distance which separates the two diffracting points. In order to evaluate the accessible contrast, we now examine the reconstruction of the two diffracting points with different electromagnetic characteristics. The two objects are characterized, respectively, by $\epsilon_{r_{s1}} = 2.5$ and $\epsilon_{r_{s2}} = 5$, 7, 9, and $\sigma_{s1} = \sigma_{s2} = 0$ S/m. The results are shown in Figs. 11 (b)–(d) and 12 (b)–(d).

2) Object Reconstruction: Our purpose is to evaluate the capability of the imaging algorithm for reconstructing objects of different shapes. Let us first consider (case 1) a dielectric rod ($\epsilon_{r_s} = 2.5$, $\sigma_s = 0$ S/m) buried in a soil characterized by $\epsilon_{r_3} = 15$, $\sigma_3 = 5 \times 10^{-2}$ S/m. The object is embedded at a depth of $3\lambda_1$, and its dimensions along the x and y directions are $L_x = 3\lambda/2$ and $L_y = \lambda_1/10$. The length of the probing line is $20\lambda_1$ and it is situated at λ_1 above the air–soil interface. The frequency of the incident plane waves varies by steps of 0.03 GHz between 2.43 GHz and 3 GHz; for each frequency, 25 incidences are used within the interval $]-\pi/2, \pi/2[$. The magnitude of the image is shown in Fig. 13 (a) (filtered at half height) and in Fig. 13 (b). The second rod has the dimensions $L_x = \lambda_1/10$ and $L_y = 3\lambda_1/2$ (rotation of 90° from the previous case), and it is illuminated with the same illumination characteristics. One notes that the obtained image (see Fig. 13 (b) and (c)) does not square exactly with the real geometry of the rod. Keeping in mind that the reconstruction process gives a representation of the polarization currents, illuminated parts of the object (i.e., the front) will be better reconstructed.

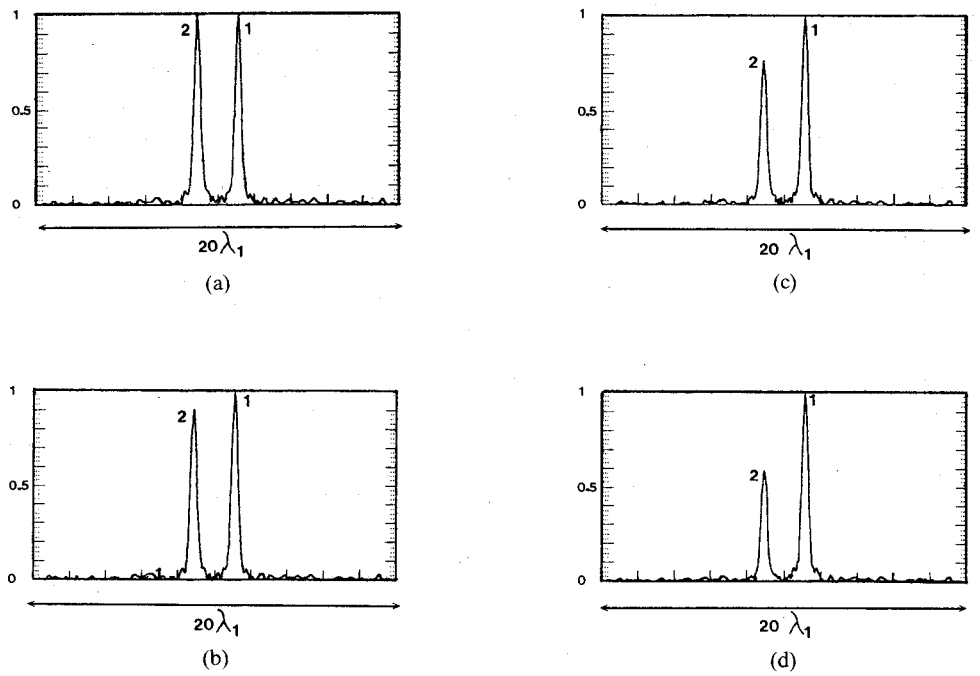

Fig. 12. Transversal sections of $|\tilde{K}(x, y)|$ corresponding to the 3-D representations shown in Fig. 11.

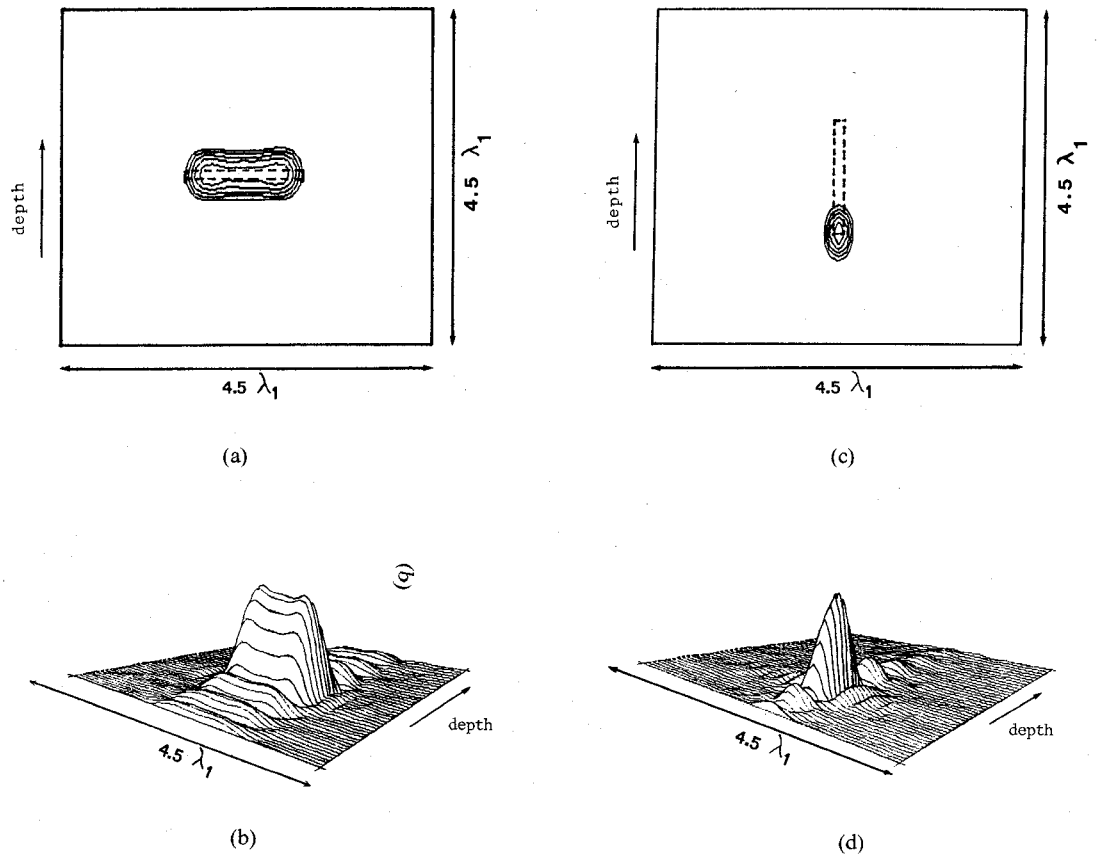

Fig. 13. Modulus of $\tilde{K}(x, y)$ for a dielectric rod ($\epsilon_{r_s} = 2.5$, $\sigma_s = 0$ S/m) parallel ((a) and (b)) and perpendicular ((c) and (d)) to the air–soil interface.

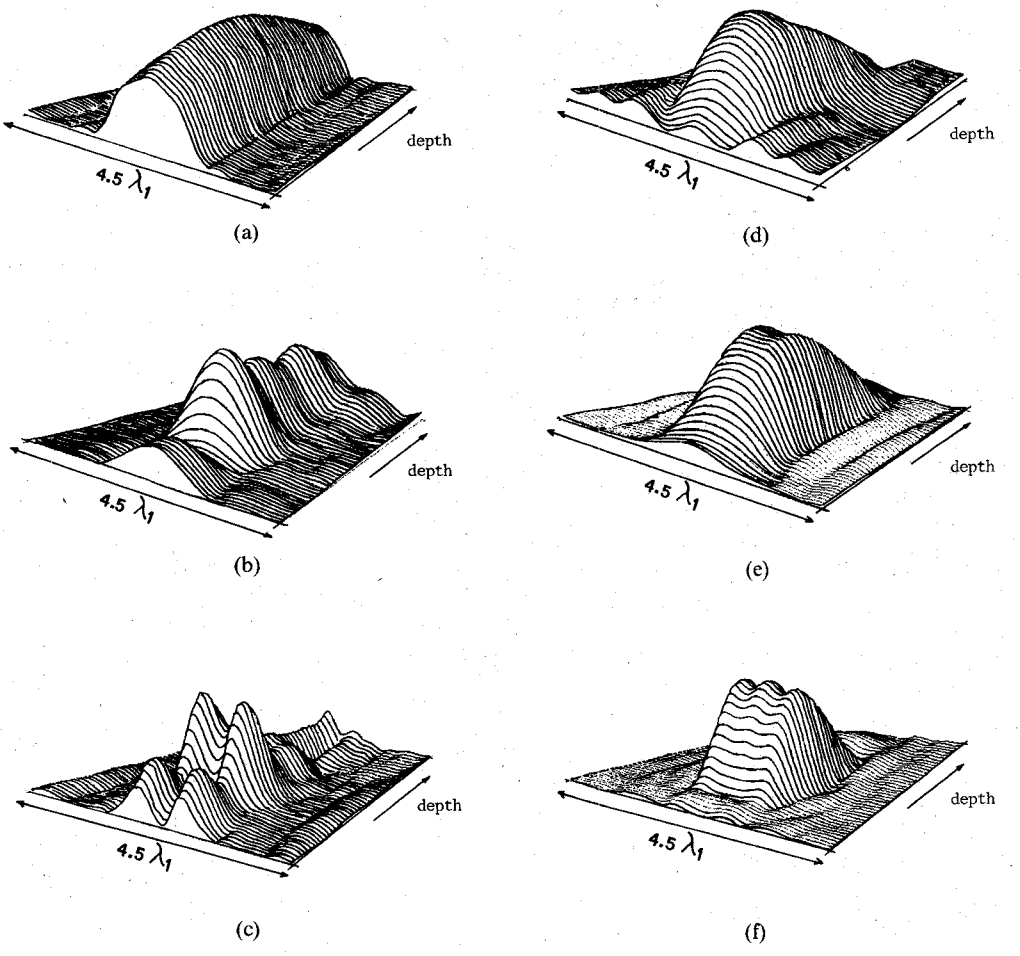

Fig. 14. 3-D representation of $|\tilde{K}(x, y)|$ obtained in the case of a homogeneous dielectric cylinder ($\epsilon_{r_s} = 3.5$, $\sigma_s = 0$ S/m) of rectangular section ($l_x = 3\lambda_1/2$, $l_y = 0.9\lambda$) in the case of two different soils. Case 1:(a), (b), (c) Loamy soil of 13.77-percent water content ($\epsilon_{r_3} = 20$, $\sigma_3 = 0.4$ S/m). Case 2: (d), (e), (f) Dry sand ($\epsilon_{r_3} = 2.55$, $\sigma_3 = 2\times10^{-3}$ S/m). $\tilde{K}(x, y)$ is obtained for (a), (d) a plane wave incidence variation in the interval $]-\pi/2, +\pi/2[$, (b), (e) for a plane wave frequency variation from 2.43 GHz to 3 GHz, and (c), (f) for both incidence and frequency variation.

In the case of the two different soils considered before —loamy soil of 13.77-percent water content (case 1: $\epsilon_{r_3} = 20$, $\sigma_3 = 0.4$ S/m) and dry sand (case 2: $\epsilon_{r_3} = 2.55$, $\sigma_3 = 2\times10^{-3}$ S/m) [27]—the object is a homogeneous rectangular cylinder with dimensions $L_x = 3\lambda_1/2$ and $L_y = 0.9\lambda_1$, characterized by $\epsilon_{r_s} = 3.5$ and $\sigma_S = 0$ S/m and buried at a depth $D = 3\lambda_1$. The length of the probing line is $20\lambda_1$, and it is situated at a distance $y_1 = \lambda_1$ above the air–soil interface. Fig. 14 shows the reconstructed object in the two cases of loamy soil (Fig. 14 (a)–(c)) and dry sand (Fig. 14 (d)–(f)).

The three representations of $|\tilde{K}(x, y)|$ are for a variation of the plane wave incidence in the interval $]-\pi/2, +\pi/2[$ with $\Delta\theta_1 = \pi/35$ (Figs. 14 (a) and (d)), for a variation of the plane wave frequency from 2.43 GHz to 3 GHz with $\Delta f = 0.03$ GHz, and for both incidence and frequency variation of the incident plane wave (Fig. 14 (e) and (f)). Fig. 15 shows the same results in magnitude filtered at half height (the images of $|\tilde{K}(x, y)|$ being represented with five highest levels over ten levels and with a relative maximum for each figure), and the geometry of the real object is drawn in dashed line. It is obvious that the object is best reconstructed when it is embedded in the dry sand because of the refraction of the plane wave at the air–soil interface; the incidence variation in case 2 provides more information about the shape of the object than in case 1. The difference between Fig. 14 (c) and (f) or Fig. 15 (c) and (f) could be explained from two factors. First, since the permittivity of the loamy soil is more important than that of the sandy soil, the information in the spectral domain for the loamy soil is more reduced and concerns higher spatial frequencies (see (28)) and the image reflects the discontinuities of the object along the y axis. Second, the conductivity of the loamy soil is higher than that of the sandy soil; the working frequency (2.43–3 GHz band) is such that the first soil–object interface is well depicted, whereas the second is not retrieved. It would be necessary to use lower frequencies for the loamy soil.

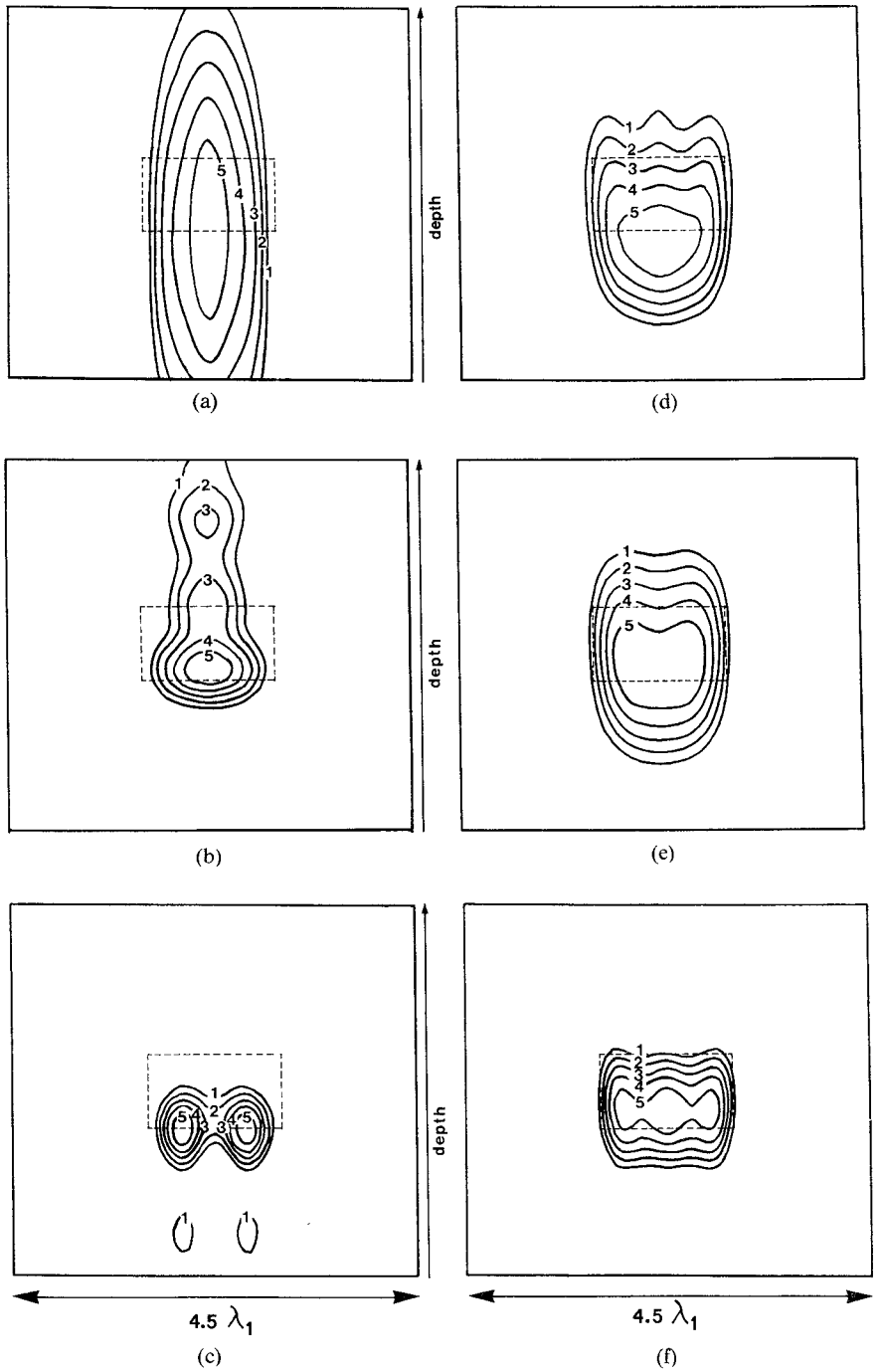

Fig. 15. 2-D representation of $|\tilde{K}(x, y)|$ filtered at half height corresponding to the same cases as in Fig. 14 (5 highest levels among 10 levels).

IV. Conclusions

Using the integral formulation of the diffracted field presented in this paper, we are able to estimate the electromagnetic response of a two-dimensional inhomogeneity buried in the earth for a plane wave excitation. We have also shown how algorithms employed in diffraction tomography can be applied to obtain images of buried objects. Simulations concerning the shape and the size of the object have been carried out for different values of soil electromagnetic parameters. The image is given by the map of $|\tilde{K}(x, y)|$ represented by means of 3-D plots. However, images based upon the phase of $\tilde{K}(x, y)$ (which needs to be unwrapped) could also be considered, for they might provide complementary information on the target. We have avoided discussing a number of details that must be taken into account in practical applications, such as the effect of a layer (water, ice, snow, etc.) and the effect of noise on the image quality.

Some of the problems to be solved in the future are the separation of the information concerning the object from soil surface reflections; the effect of noise and of a strati-

fied ground on image quality; and the application of this method in a three-dimensional problem.

APPENDIX

A line source is located at a point (x', y') with $y' > 0$ in a soil characterized by ϵ_{r_3}, σ_3; (x, y) denotes the observation point where the field must be evaluated. The Green's function satisfies

$$\Delta_{xy}G(x, y; x', y') + k_1^2 G(x, y; x', y') = 0, \qquad (y < 0)$$

$$\Delta_{xy}G(x, y; x', y') + k_3^2 G(x, y; x', y') = -\delta(x - x', y - y'), \qquad (y > 0) \quad \text{(A1)}$$

where $\delta(x, y)$ denotes the bidimensional Dirac distribution centered at (0,0) and Δ_{xy} is a scalar Laplacian operator defined by

$$\Delta_{xy} = \frac{\partial^2}{\partial x^2} + \frac{\partial^2}{\partial y^2}.$$

Let $g(\nu, y; x', y)$ be the Fourier transform of $G(x, y; x', y')$ with respect to x. Thus

$$G(x, y; x', y') = \int_{-\infty}^{+\infty} g(\nu, y; x', y') e^{2i\pi\nu x}\, d\nu \quad \text{(A2)}$$

is the system (A1) is equivalent to

$$\frac{\partial^2 g}{\partial y^2} + \tilde{\gamma}_1^2 g = 0 \qquad (\text{for } y > 0)$$

$$\frac{\partial^2 g}{\partial y^2} + \tilde{\gamma}_3^2 g = -\delta(y - y') e^{-2i\pi\nu x'} \qquad (\text{for } y < 0) \quad \text{(A3)}$$

with

$$\tilde{\gamma}_j^2 = k_j^2 - 4\pi^2\nu^2, \qquad j = 1,3.$$

Solutions of system (A2) are given by

$$\begin{aligned} g &= B_1 e^{-i\tilde{\gamma}_1 y} && (\text{for } y < 0) \\ g &= A_3 e^{i\tilde{\gamma}_3 y} + B_3 e^{-i\tilde{\gamma}_3 y} && (\text{for } 0 < y < y') \\ g &= A_4 e^{i\tilde{\gamma}_3 y} && (\text{for } y > y'). \end{aligned} \quad \text{(A4)}$$

B_1, A_3, B_3, A_4 are given by the boundary conditions:

1) continuity of g for $y = 0$ and $y = y'$;
2) continuity of $\partial g/\partial y$ for $y = 0$; and
3) discontinuity of $\partial g/\partial y$ for $y = y'$.

Thus,

$$\left.\frac{\partial g}{\partial y}\right|_{y \to y'^+} - \left.\frac{\partial g}{\partial y}\right|_{y \to y'^-} = e^{2i\pi\nu x'}. \quad \text{(A5)}$$

These boundary conditions are determined by the following relation:

$$f'' = \{f''\} + \sum_{i=1}^{n} \sigma_{if'}\delta(x - x_i) + \sigma_{if}\delta'(x - x_i) \quad \text{(A6)}$$

between the second derivative taken in the distribution sense f'' and the second derivative taken in the function sense $\{f''\}$ for a function f which admits finite discontinuities at points x_i $(i = 1, \ldots, n)$, where σ_{if} and $\sigma_{if'}$ are given by

$$\sigma_{if} = f(x_i^+) - f(x\bar{i})$$

$$\sigma_{if'} = f'(x_i^+) - f'(x\bar{i})$$

and $\delta(x - x_i)$, $\delta'(x - x_i)$ and f' denote, respectively, the Dirac distribution centered at x_i, its first derivative, and the first derivative of f.

Solving the boundary conditions, one obtains

$$B_1 = \frac{i}{\tilde{\gamma} + \tilde{\gamma}_3} e^{i\tilde{\gamma}_3 y'} e^{-2i\pi\nu x'}$$

$$A_3 = \frac{i}{2\tilde{\gamma}_3} \frac{(\tilde{\gamma}_3 - \tilde{\gamma}_1)}{(\tilde{\gamma}_3 + \tilde{\gamma}_1)} e^{i\tilde{\gamma}_3 y'} e^{-2i\pi\nu x'}$$

$$B_3 = \frac{i}{2\tilde{\gamma}_3} e^{i\tilde{\gamma}_3 y'} e^{-2i\pi\nu x'}$$

$$A_4 = \frac{i}{2\tilde{\gamma}_3}\left[\frac{(\tilde{\gamma}_3 - \tilde{\gamma}_1)}{(\tilde{\gamma}_3 + \tilde{\gamma}_1)} e^{i\tilde{\gamma}_3 y'} + e^{-i\tilde{\gamma}_3 y'}\right] e^{-2i\pi\nu x'} \quad \text{(A7)}$$

and finally

$$g(\nu, y; x', y') = \frac{i}{(\tilde{\gamma}_1 + \tilde{\gamma}_3)} e^{i\tilde{\gamma}_3 y'} e^{-i\tilde{\gamma}_1 y} e^{-2i\pi\nu x'} \qquad (\text{for } y < 0)$$

$$g(\nu, y; x', y') = \frac{i}{2\tilde{\gamma}_3}\left[e^{i\tilde{\gamma}_3|y - y'|} + \frac{(\tilde{\gamma}_3 - \tilde{\gamma}_1)}{(\tilde{\gamma}_3 + \tilde{\gamma}_1)} e^{i\tilde{\gamma}_3(y + y')}\right] \cdot e^{-2i\pi\nu x'} \qquad (\text{for } y > 0) \quad \text{(A8)}$$

which yields $G(x, y; x', y')$ upon substitution of (A8) into (A2).

REFERENCES

[1] P. J. B. Clarricoats, "Portable radar for the detection of buried objects," in *Radar '77—IEEE Int. Conf.* (London, England), pp. 547–551.

[2] Keigo Iizuka and Alois P. Freundofer, "Detection of nonmetallic buried objects by a step frequency radar," *Proc. IEEE*, vol. 71, pp. 276–279, Feb. 1983.

[3] Luen C. Chan, David L. Moffatt, and Leon Peters, "A characterization of subsurface radar targets," *Proc. IEEE*, vol. 67, pp. 991–1000, July 1979.

[4] Luen C. Chen *et al.*, "Improved performance of a subsurface radar target identification system through antenna design," *IEEE Trans. Antennas Propagat.*, vol. AP-29, pp. 307–311, Mar. 1981.

[5] A. Blanchard, "Utilisation d'un radar impulsionnel pour l'étude des structures," *Revue Pratique de Contrôle Industriel*, vol. 127, pp. 86–88, 1984.

[6] P. J. Richards and A. P. Anderson, "Microwave images of subsurface utilities in an urban environment," in *Proc. 8th European Microwave Conf.*, 1978, pp. 33–37.

[7] N. Osumi and K. Ueno, "Microwave holographic imaging method with improved resolution," *IEEE Trans. Antennas Propagat.*, vol. AP-32, pp. 1018–1026, Oct. 1984.

[8] N. Osumi and K. Ueno, "Microwave holographic imaging of underground objects," *IEEE Trans. Antennas Propagat.*, vol. AP-33, pp. 152–159, Feb. 1985.

[9] J. C. Bolomey *et al.*, "A quasi real time microwave inverse scattering technique applicable to biomedical tomography," in *Proc. URSI Symp. Nat. Radio Sci. Meet.*, 1982, p. 93.

[10] J. C. Bolomey, A. Izadnegahdar, L. Jofre, C. Pichot, G. Peronnet, and M. Solaimani, "Microwave diffraction tomography for biomedical applications," *IEEE Trans. Microwave Theory Tech.*, vol. 30, pp. 1998–2000, Nov. 1982.

[11] C. Pichot, L. Jofre, G. Peronnet, and J. C. Bolomey, "Active microwave imaging of inhomogeneous bodies," *IEEE Trans. Antennas Propagat.*, vol. AP-33, pp. 416–425, Apr. 1985.
[12] B. Duchene, D. Lesselier, and W. Tabbara, "Diffraction tomography approach to acoustical imaging and media characterization," *J. Opt. Soc. Amer. A*, vol. 2, pp. 1943–1953, Nov. 1985.
[13] Samir F. Mahmoud, Sami M. Ali, and James R. Wait, "Electromagnetic scattering from a buried cylindrical inhomogeneity inside a lossy earth," *Radio Sci.*, vol. 16, no. 6, pp. 1285–1298, Nov.–Dec. 1981.
[14] J. H. Richmond, "Scattering by a dielectric cylider of arbitrary cross-section shape," *IEEE Trans. Antennas Propagat.*, vol. AP-13, no. 3, pp. 334–341, May 1965.
[15] S. X. Pan and Avinash C. Kak, "A computational study of reconstruction algorithms for diffraction tomography: Interpolation versus filtered backpropagation," *IEEE Trans. Acoust., Speech, Signal Processing*, vol. ASSP-31, no. 5, pp. 1262–1275, Oct. 1983.
[16] A. J. Devaney, "A computer simulation study of diffraction tomography," *IEEE Trans. Biomed. Eng.*, vol. BME-30, pp. 377–386, July 1983.
[17] J. Detlefsen, "The resolution limits of the imaging of conducting bodies using multistatic scattering," *IEEE Trans. Antennas Propagat.*, vol. AP-28, no. 3, pp. 377–380, May 1980.
[18] R. F. Harrington, *Field Computation by Moment Methods*. New York: McGraw-Hill, 1968.
[19] J. H. Richmond, "TE-wave scattering by a dielectric cylinder of arbitrary cross section shape," *IEEE Trans. Antennas Propagat.*, vol. AP-14, pp. 460–464, July 1966.
[20] M. M. Ney, S. S. Stuchly, A. M. Smith, and M. Goldberg, "Electromagnetic imaging using moment methods," in *Proc. URSI Symp. on Electromagnetic Theory*, 1983, pp. 281–284.
[21] Gerald W. Hohmann, "Electromagnetic scattering by conductors in the earth near a line source of current," *Geophysics*, vol. 36, no. 1, pp. 101–131, Feb. 1971.
[22] A. Dey and H. F. Morrisson, "Electromagnetic response of two dimensional inhomogeneities in a dissipative half space for Turam interpretation," *Geophys. Prospecting*, vol. 21, pp. 340–365, June 1973.
[23] R. M. Mersereau and A. V. Oppenheim, "Digital reconstruction of multidimensional signals from their projections," *Proc. IEEE*, vol. 62, pp. 210–229, Oct. 1974.
[24] Robert M. Levitt, "Reconstruction algorithms: Transform methods," *Proc. IEEE*, vol. 71, pp. 390–408, Mar. 1983.
[25] J. Anthony Parker, Robert V. Kenyon, and Donald E. Troxel, "Comparison of interpolating methods for image resampling," *IEEE Trans. Med. Imaging*, vol. MI2, no. 1, pp. 31–39, Mar. 1983.
[26] Jackie E. Hipp, "Soil electromagnetic parameters as functions of frequency, soil density and soil moisture," *Proc. IEEE*, vol. 62, pp. 98–103, Jan. 1974.
[27] Arthur R. von Hippel, *Dielectric Materials and Their Applications*. Cambridge, MA: MIT Press, 1954.
[28] Martti T. Hallikainen *et al.*, "Microwave dielectric behavior of wet soil—Part I: Empirical models and experimental observations," *IEEE Trans. Geosci. Remote Sensing*, vol. GE-23, no. 1, pp. 25–34, Jan. 1985.
[29] Martti T. Hallikainen *et al.*, "Microwave dielectric behavior of wet soil–Part II: Dielectric mixing models," *IEEE Trans. Geosci. Remote Sensing*, vol. GE-23, no. 1, pp. 35–46, Jan. 1985.
[30] Frederic J. Harris, "On the use of windows for harmonic analysis with the discrete Fourier transform," *Proc. IEEE*, vol. 66, pp. 51–83, Jan. 1978.
[31] Christian Pichot and Luc Chommeloux, "Algorithms for active microwave imaging—Biomedical and civil engineering applications," presented at U.S.–France Conf. on Near Field Microwave Imaging, Atlanta, GA, June 10–11, 1985.

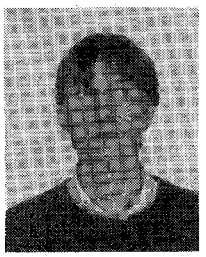

Luc Chommeloux was born in Longué, France, on April 16, 1960. He received the Maitrise degree in physics and the Diplôme d'Etudes Approfondies in optics from the University of Paris-Sud (Orsay) in 1982 and 1983, respectively.

He is currently working toward the Doctorat degree on the diagnostics of embedded objects and its application to civil engineering applications. His fields of interest are direct and inverse problems in electromagnetism.

✠

Christian Pichot was born in Rozay-en-Brie, France, on March 6, 1951. He received the M.S. degree from the University of Nice, France, in 1974 and the Doctorat de Troisième Cycle and the Doctorat ès Sciences degrees from the University of Paris-XI (Orsay) in 1977 and 1982, respectively.

He joined the Groupe d'Electromagnétisme of the Laboratoire des Signaux et Systèmes in 1978. He is presently a Chargé de Recherche at the Centre National de la Recherche Scientifique (C.N.R.S.). His research activities are concerned with scattering, direct and inverse, and guided wave problems in inhomogeneous media. Since 1981, he has been involved in microwave imaging for biomedical applications and, since 1983, for civil engineering applications.

Dr. Pichot received the Microwave Prize of the European Microwave Conference in Nuremberg (F.R.G.) in 1983.

✠

Jean-Charles Bolomey was born in Paris, France, in 1942. He received the electrical engineering degree from the École Supérieure d'Electricité in 1963 and the Ph.D. degree from the University of Paris-XI (Orsay) in 1971.

He became Assistant Professor in 1974 and Professor in 1976 at the University Paris-XI (Orsay). His research activity, conducted in the Groupe d'Electromagnétisme (CNRS-ESE) since that time, has been devoted to general scattering and diffraction, both numerical and experimental aspects. Since 1981, his main field of interest has been in near-field imaging with a special emphasis on biomedical applications and antenna testing.

Dr. Bolomey received the Blondel medal of the Société des Electriciens et des Electroniciens in 1976, the General Ferié Prize de l'Académie des Sciences in 1984 and, with his group, the Microwave Prize of the European Microwave Conference in Nuremberg in 1983. From 1977 to 1982, he was President of Section 25 (ondes et signaux) of the Société des Electriciens et des Electroniciens, and from 1978 to 1984, he served as the French delegate to Commission B of the International Union of Radio Science.